Title

Optimal variable flip angle schemes for dynamic acquisition of exchanging hyperpolarized substrates

Authors

Xing, Yan
Reed, Galen D
Pauly, John M
et al.

Publication Date

2013-09-01

DOI

10.1016/j.jmr.2013.06.003

Peer reviewed

Published in final edited form as:
J Magn Reson. 2013 September ; 234: 75–81. doi:10.1016/j.jmr.2013.06.003.

Optimal Variable Flip Angle Schemes For Dynamic Acquisition Of Exchanging Hyperpolarized Substrates

Yan Xing[1], **Galen D. Reed**[1], **John M. Pauly**[2], **Adam B. Kerr**[2], and **Peder E. Z. Larson**[1,*]

[1]Department of Radiology and Biomedical Imaging, University of California - San Francisco, San Francisco, California

[2]Magnetic Resonance Systems Research Laboratory, Department of Electrical Engineering, Stanford University, Stanford, California

Abstract

In metabolic MRI with hyperpolarized contrast agents, the signal levels vary over time due to T_1 decay, T_2 decay following RF excitations, and metabolic conversion. Efficient usage of the nonrenewable hyperpolarized magnetization requires specialized RF pulse schemes. In this work, we introduce two novel variable flip angle schemes for dynamic hyperpolarized MRI in which the flip angle is varied between excitations and between metabolites. These were optimized to distribute the magnetization relatively evenly throughout the acquisition by accounting for T_1 decay, prior RF excitations, and metabolic conversion. Simulation results are presented to confirm the flip angle designs and evaluate the variability of signal dynamics across typical ranges of T_1 and metabolic conversion. They were implemented using multiband spectral-spatial RF pulses to independently modulate the flip angle at various chemical shift frequencies. With these schemes we observed increased SNR of [1-^{13}C]lactate generated from [1-^{13}C]pyruvate, particularly at later time points. This will allow for improved characterization of tissue perfusion and metabolic profiles in dynamic hyperpolarized MRI.

Introduction

Magnetic resonance imaging (MRI) with hyperpolarized ^{13}C agents provides the unique ability to non-invasively probe in vivo metabolism [1, 2, 3]. It has significant potential to improve the detection and characterization of cancer in individual patients [4, 5, 6, 7, 8, 9, 10, 11, 12, 13, 14], and may also have clinical applications in other metabolic disorders, such as ischemic heart disease [15, 16, 17] and inflammation [18]. This information can be used to determine the severity of disease, as well as monitor the progression and response to therapy [6, 8, 9, 10, 13, 14]. Hyperpolarized [1-^{13}C]pyruvate kinetics are particularly informative about cancer biology: pyruvate-lactate conversion can be used to discern cancerous from healthy tissues and to monitor cancer progression [4].

Dissolution dynamic nuclear polarization (DNP) increases the injected substrate signal more than 10,000-fold, creating a hyperpolarized state that provides sensitivity improvements

*Address Correspondence to: Peder E. Z. Larson, Byers Hall, Room 102C, 1700 4th St, San Francisco, CA 94158, TEL: (415) 514-4876, peder.larson@ucsf.edu.

over conventional MRI or MR spectroscopy. The hyperpolarized magnetization is in a highly non-equilibrium state, and decays back to thermal equilibrium with the longitudinal relaxation time, T_1. Furthermore, magnetization is lost due to transverse relaxation (T_2) following creation of transverse magnetization following radio-frequency (RF) excitations. The rapid loss of the nonrenewable polarization necessitates rapid and efficient imaging methods.

Specifically, hyperpolarized MR requires specialized RF excitation schemes for efficient usage of the magnetization, a number of which have been developed to date. Variable flip angle ("vfa") schemes have been designed to account for losses due to RF excitation and T_1 relaxation across multiple excitations [19, 20]. RF pulses using multiple spectral bands ("multiband") with different flip angles to account for metabolic conversion have been used for dynamic hyperpolarized ^{13}C imaging, demonstrating improved observation of metabolic products and kinetics by minimally exciting the substrate magnetization [21, 22, 23, 24]. Independent control of metabolite flip angles has also been implemented in metabolite-specific imaging with spectral-spatial RF pulses, including for monitoring the arrival of [1-^{13}C]pyruvate and conversion to ^{13}C-bicarbonate and [1-^{13}C]lactate with varying flip angles across time [25] and for measuring kinetics with saturation transfer [26].

This paper presents two novel variable flip angle schemes for dynamic hyperpolarized imaging that account for metabolic conversion as well as losses due to RF excitation and T_1 relaxation by independently controlling the flip angle of individual metabolites. We implemented this using multiband spectral-spatial RF excitation pulses for monitoring the conversion from [1-^{13}C]pyruvate to [1-^{13}C]lactate in vivo. The new variable flip angle schemes distribute the nonrenewable hyperpolarized magnetization relatively evenly throughout a dynamic acquisition, which increases the temporal window. They were designed for dynamic acquisitions that measure the metabolic tracer and conversion kinetics. These approaches could also be applied for reducing blurring due to T_1 and metabolic conversion during longer (> 5 sec) imaging acquisitions. The first scheme uses effective relaxation rates to distribute the magnetization ("*T1-effective*"); the second scheme uses numerically optimized flip angles to maintain constant signal over the duration of acquisition ("*const-signal*").

Theory

Previous variable flip angle (vfa) schemes proposed that the pulse flip angle can be progressively increased during the course of the acquisition in hyperpolarized MR to account for losses due to RF excitation and T_1 relaxation and maintain a flat signal response [19, 20]. In this method, the flip angle, θ [n], for the nth flip angle, is given by:

$$\theta[n]=\cos^{-1}\sqrt{\frac{E_1^2-E_1^{2(N-n+1)}}{1-E_1^{2(N-n+1)}}}, \quad (1)$$

$$E_1=\exp\left(-\frac{TR}{T_1}\right) \quad (2)$$

where N is the total number of excitation pulses. In this way, the last flip angle generated by this algorithm will be a 90° pulse, which utilizes all of the remaining polarization.

In this work, we additionally account for metabolic conversion by independently varying the flip angle of individual metabolites based on their conversion rates. We considered the case of hyperpolarized [1-^{13}C]pyruvate converting to [1-^{13}C]lactate. (This is directly generalized

to any substrate to product conversion, see Discussion.) Their magnetization can be quantified using a two-site exchange model:

$$\frac{d}{dt}\begin{bmatrix} P(t) \\ L(t) \end{bmatrix} = \begin{bmatrix} -\frac{1}{T_{1P}} - K_{PL} & 0 \\ K_{PL} & -\frac{1}{T_{1L}} \end{bmatrix} \begin{bmatrix} P(t) \\ L(t) \end{bmatrix} \quad (3)$$

where $P(t)$ and $L(t)$ are the hyperpolarized magnetizations of pyruvate and lactate, respectively, at time, t, K_{PL} is the metabolic conversion rate from pyruvate to lactate, and we assumed that the back conversation rate from lactate to pyruvate is negligible.

Integrating equation (3) over the acquisition time, with the simplification to a matrix A:

$$A = \begin{bmatrix} -\frac{1}{T_{1P}} - K_{PL} & 0 \\ K_{PL} & -\frac{1}{T_{1L}} \end{bmatrix} \quad (4)$$

We obtain:

$$\begin{bmatrix} P(t) \\ L(t) \end{bmatrix} = e^{-A \cdot t} \begin{bmatrix} P(0) \\ L(0) \end{bmatrix}. \quad (5)$$

Methods

In our *T1-effective* scheme, we observed that pyruvate and lactate in the model in equation (5) have approximate relaxation rates of $R_{1P,eff} = \frac{1}{T_{1P}} + K_{PL}$ (including additional losses for conversion to lactate) and $R_{1L,eff} = \frac{1}{T_{1L}} - K_{PL}$ (including magnetization gained from conversion), respectively. In this scheme, we calculated the flip angles, $\theta_X[n]$ for metabolite X (ie pyruvate, lactate) as in Equation (1), but with these approximate relaxation rates:

$$\theta_X[n] = \cos^{-1}\sqrt{\frac{E_{1,X}^2 - E_{1,X}^{2(N-n+1)}}{1 - E_{1,X}^{2(N-n+1)}}} \quad (6)$$

$$E_{1,P} = \exp\left(-TR\left(\frac{1}{T_{1P}} + K_{PL}\right)\right) \quad (7)$$

$$E_{1,L} = \exp\left(-TR\left(\frac{1}{T_{1L}} - K_{PL}\right)\right) \quad (8)$$

For the *const-signal* scheme, we numerically optimized the flip angles of pyruvate and lactate for constant signal amplitude during the scan assuming both T_1 relaxation and metabolic conversion. With the *T1-effective* scheme, pyruvate already maintains a constant signal level in our two-site exchange model; thus the same pyruvate flip angles from Equations 6 and 7 were used in this scheme. The optimization of the lactate flip angles was determined by an empirical approach, where a constant signal level (S_{test}) was assumed and the corresponding flip angles were calculated as:

$$\theta_L[n]=sin^{-1}\left(\frac{S_{test}}{M_L[n-1]}\right) \quad (9)$$

where $M_L[n]$is the remaining lactate magnetization after pulse n. S_{test} was iteratively refined until the maximal available magnetization has been utilized, signified by a negligible amount of magnetization of lactate by the end of acquisition and a final flip angle of 90°.

All simulations and flip angle designs were performed in MATLAB (The Mathworks Inc., Natick, MA). A library of spectral-spatial RF excitation pulses was created using the Spectral-Spatial RF Pulse Design package for MATLAB [21, 27] (available at http://rsl.stanford.edu/research/software.html). MATLAB scripts for the two design schemes are available online at http://www.radiology.ucsf.edu/research/labs/larson/software.

Flip angle designs with our new schemes for comparison to prior methods in simulation and normal rat experiments used the following design parameters: initial magnetizations of $P(0) = 1$ and $L(0) = 0.05$ (accounting for some lactate build up by the start of the acquisition); longitudinal relaxation times (T_1) of 25 seconds for both pyruvate and lactate, even though the actual T_1 values may vary significantly with the surrounding environment and may differ between pyruvate and lactate [28]; $K_{PL} = 0.025\ s^{-1}$ based on previous simulation [29] and experimental [8] results; repetition time, TR = 1 s; and a total acquisition time of 44 s was chosen for the effective utilization of magnetization and detectable signal level.

Experiments were performed in normal rats and in a transgenic adenocarcinoma of mouse prostate (TRAMP) mouse model on a 3 Tesla clinical-research MRI system (GE Healthcare, Waukesha, WI, USA) with 40 mT/m, 150 mT/m/ms gradients and a broadband RF amplifier. All animal studies were carried out under a protocol approved by our Institutional Animal Care and Use Committee. The animals were placed on a 37°C heating pad in the RF coil, and anesthesia was maintained by a continual delivery of isoflurane (1–1.5%) with oxygen (1 liter/min). Respiratory rate and skin color were monitored by periodic visual inspection. A custom built, dual-tuned mouse birdcage coil was used for RF transmission and signal reception [30]. Compounds consisting of neat [1-^{13}C] pyruvic acid (14.2 M) with the trityl radical OX063 (15 mM) (Oxford Instruments, UK), and 99% ^{13}C -urea (Sigma-Aldrich, St. Louis, MO) in glycerol (6.4 M) with the trityl radical OX063 (23 mM), were polarized in a HyperSense DNP system (Oxford Instruments, Abingdon, UK) at 3.35 T and a temperature of 1.3° K. The hyperpolarized compounds were dissolved in a TRIS/NaOH/EDTA buffer to produce a solution with neutral pH that was injected into the animals. The pH was measured from a separate aliquot of this solution.

The normal rat experiments used a 2.6 mL injection over 12 s of 100 mM [1-^{13}C]pyruvate. Data acquisition of dynamic ^{13}C -spectra began 13 s after the start of injection, and were acquired over a 4 cm slab containing kidneys and liver with echo time, TE = 50 ms, an adiabatic double spin-echo [31], TR = 1 s, and 44 repetitions. The data was normalized by the initial pyruvate flip angle divided by the initial pyruvate peak height to account for differences in polarization between injections. The metabolite peak heights were fit to the two-site exchange parameters using non-linear least squares fitting in MATLAB. The fitting routine included scaling factors to account for the various RF flip angles.

The TRAMP experiments used a 350 μL injection over 12 s of 80 mM [1-^{13}C]pyruvate and 80 mM ^{13}C-urea [32]. 3D dynamic magnetic resonance spectroscopic imaging (MRSI) was acquired using a compressed-sensing echo-planar spectroscopic imaging (EPSI) sequence as described in [23]. To summarize, the sequence had: a spectral resolution of 9.83 Hz and a 581 Hz spectral bandwidth to include all metabolites of interest; TE = 160ms, TR = 250ms; 12×12×16 matrix, 5×5×5.4 mm resolution (0.135 cc); time resolution of 2 s. For these

experiments, a *T1-effective* dynamic variable flip angle scheme was generated using K_{PL} = 0.025 1/s, $T_{1P} = T_{1L} = \infty$, 44 s total acquisition time, and was compared to a constant 6 (pyruvate & urea) and 12 (lactate & alanine) degree multiband excitation [23].

Results

Simulations

Sample flip angles and simulated signals are shown in Figure 1. The new schemes theoretically lead to increased metabolite signal at the end of the dynamic acquisition, and utilize all of the available magnetization. Lactate signal in the *T1-effective* scheme is not particularly flat for the first 20 s because the change in lactate magnetization is dominated by K_{PL}. However, it is nearly flat after 20 s because T_{1L} becomes a larger effect and the change lactate is closer to $R_{1L,eff}$.

Figure 2 shows the spectral profiles for three different spectral-spatial RF pulses that were designed for the *T1-effective* flip angles in Fig. 1. These designs included spectral bands for pyruvate, lactate, alanine, and urea, where the urea flip angle was set to be the same as pyruvate and the alanine flip angle to be the same as lactate. The spectral profiles show that the pulse design specifications, which included a flip angle variation (ie ripple) tolerance of 1/30th the flip angle, were achieved with the multiple frequency excitation bands and their variations across time.

It is important to understand the effect of T_1 relaxation, metabolic conversion, and initial lactate magnetization on the simulation results, as the experimental values may vary from the design values used to generate the flip angles. Simulations performed with ± 20% deviations from the design T_1 (25 s), ±50% deviations from the design K_{PL} (0.025 s^{-1}), and ±50% deviations from the design initial lactate magnetization ($L(0) = 0.05$ for $P(0) = 1$) are shown in Figure 3. These simulation results show how variation in experimental parameters within a voxel will lead to deviations in the locally observed dynamics. In particular, the dynamics for both schemes vary significantly with changes in K_{PL}, allowing for distinction of regions with high metabolic activity such as cancer. However, they are also sensitive to differences in T_1. The *const-signal* scheme appears more sensitive to differences in the initial magnetization levels because it applies a large initial flip angle, while the *T1-effective* approach only has small shifts in the curve heights.

Experiments

The flip angle schemes were tested in vivo in a normal rat, the results of which are shown in Fig. 4. The new schemes resulting in improved signal at later time points, particularly for the metabolic products due to the more efficient use of the magnetization. They led to a nearly constant pyruvate signal that was identical for both schemes, as predicted by simulation. The *T1-effective* scheme also showed relatively flat lactate and alanine signal curves. However, unlike simulation, these metabolites had a non-flat response for the *const-signal* scheme due to differences between the actual T_1, K_{PL}, and initial magnetization values and those used in designed the flip angles (Fig. 3). In particular, the simulation results in Fig. 3c show that this scheme is sensitive to the initial magnetization levels, suggesting that the in vivo initial levels were higher than expected which led to very high initial signal values. This was confirmed through kinetic model fitting in Table 1, where the fitted initial product metabolite signal levels were almost 2-fold higher than expected by the design. Also, the fitted relaxation times were shorter and the conversion rate was less than those used in the design, which explains the deviation of these curves from the predicted signal curves. Such model fitting can be used for future refinements of the flip angle design parameters. (The

alanine initial values were unexpectedly different between experiments, which could be due to alanine metabolism differences during the ~3 hours the animal was anesthetized.)

A *T1-effective* dynamic variable flip angle scheme that only compensated for estimated metabolic conversion ($T_1 = \infty$) was designed to provide a balance of temporal window and SNR for the 3D dynamic compressed sensing MRSI acquisition in Fig. 5 [23]. (Using $T_1 < \infty$ resulted in smaller initial flip angles for which the metabolite signals were below the noise, data not shown.) Both flip angle schemes used identical flip angles for pyruvate and urea, and for lactate and alanine. The variable flip angle scheme led to an increased temporal window for all metabolites over previously used constant flip angle schemes. Having a greater number of images with detectable signal is particularly beneficial to improve the quality of the compressed sensing reconstruction. The lactate and alanine signal was greater over most of the experiment duration, while the pyruvate and urea signal was greater at later time points. Alanine was primarily observed in the liver, as thus was not shown for the kidneys and prostate tumor regions. This in vivo result demonstrates the value of dynamic variable flip angles schemes that account for metabolic conversion.

Discussion

In this work, we optimized the spectrally-selective flip angles for a constant signal across excitations. This was done in order to evenly distribute the available hyperpolarized magnetization between dynamic images and increase the temporal window. This increased window improved the 3D dynamic compressed sensing MRSI reconstruction. This would also reduce signal variation between TRs that can cause blurring or ghosting artifacts. A constant signal was chosen to demonstrated this principle because it was a straightforward parameter to optimize, but other signal modulations are possible. For example, we had improved results even without accounting for T_1 (Fig. 5), which does not theoretically result in a constant signal.

The two schemes presented require very similar inputs, with the *const-signal* requiring an estimate of the initial magnetization. As shown in Fig. 3, both schemes are sensitive to changes in the metabolic conversion rate, which is very important to distinguish cancerous and normal tissues. There are also both sensitive to changes in T_1, which could vary based on the local metabolite environment or flow in and out of a voxel. The *const-signal* scheme is more sensitive to the initial magnetization than the *T1-effective* scheme because it uses larger initial flip angles. It may not be desirable to be sensitive to the initial magnetization as this depends on the acquisition timing.

All parameters can be fit with kinetic modeling. However, as shown in Table 1, the kinetic model fits unexpectedly varied between the four acquisitions. We believe this is due to instabilities when fitting a two-site exchange model with noisy data [33]. For this reason, future work will thoroughly investigate which flip angle schemes result in the most accurate kinetic modeling.

In the TRAMP study, we used $T_1 = \infty$ in the flip angle designs because otherwise the initial flip angles for the chosen acquisition TR and duration were too small to observe the metabolites. However, there was still an improvement in temporal window, particularly for the metabolic products, when using the *T1-effective* variable flip angle scheme. When using design $T_1 < \infty$, the total acquisition duration will be limited because the initial flip angles will become smaller.

The schemes can readily be extended to include substrate conversion to a second product, such as [1-^{13}C]pyruvate to [1-^{13}C]alanine. For the *T1-effective* scheme, the effective

relaxation rates simply become: $R_{1P,eff}=\frac{1}{T_{1P}}+K_{PL}+K_{PA}$, $R_{1A,eff}=\frac{1}{T_{1A}}-K_{PA}$, and $R_{1L,eff}$ remains the same, where K_{PA} is the conversion rate from pyruvate to alanine. For the *const-signal* scheme, the pyruvate flip angles are the same as the *T1-effective*, and the alanine flip angle can be numerically optimized identically to lactate using equation (9).

While this manuscript focused on [1-^{13}C]pyruvate to [1-^{13}C]lactate conversion, the methods are generalizable to other compounds. They can be directly applied for any substrate to product(s) conversion with negligible back conversion rates. Also, while we used multiband RF excitation pulses, these schemes could be implemented using spectrally selective pulses in metabolite-specific imaging [34].

When the back conversion is not negligible, the *T1-effective* relaxation rates can be modified as (eg for pyruvate and lactate): $R_{1P,eff}=\frac{1}{T_{1P}}+K_{PL}-K_{LP}$ and $R_{1L,eff}=\frac{1}{T_{1L}}-K_{PL}+K_{LP}$, where K_{LP} is the conversion rate from lactate to pyruvate. To obtain a constant signal, a more complex numerical optimization of the flip angles would be required.

Conclusion

A flip angle scheme that varies not only over time but also between metabolites is beneficial for improving the detected signal in hyperpolarized metabolic imaging experiments. We have described two variable flip angle schemes with multiband RF pulses that can account for T_1 decay, prior RF excitations, and metabolic conversion. The in vivo results demonstrated the improved performance of these schemes for extending the temporal window in dynamic hyperpolarized ^{13}C imaging, which will in turn improve the characterization of tissue perfusion and metabolic profiles.

Acknowledgments

The authors acknowledge Dr. James Tropp for the ^{1}H/^{13}C rodent coils used in all experiments. We would also like to thank Dr. Robert Bok for assistance performing the experiments and Dr. Dan Vigneron for his invaluable support of this work. This work was supported by NIH grants R00- EB012064, P41-EB013598, and P41-EB015891.

References

1. Ardenkjær-Larsen JH, Fridlund B, Gram A, Hansson G, Hansson L, Lerche MH, Servin R, Thaning M, Golman K. Increase in signal-to-noise ratio of >10,000 times in liquid-state NMR. Proc Natl Acad Sci U S A. 2003; 100:10158–10163. [PubMed: 12930897]
2. Golman K, Ardenkjær -Larsen JH, Petersson JS, Månsson S, Leunbach I. Molecular imaging with endogenous substances. Proc Natl Acad Sci U S A. 2003; 100:10435–10439. [PubMed: 12930896]
3. Golman K, in 't Zandt R, Thaning M. Real-time metabolic imaging. Proc Natl Acad Sci U S A. 2006; 103:11270–11275. [PubMed: 16837573]
4. Kurhanewicz J, Vigneron DB, Brindle K, Chekmenev EY, Comment A, Cunningham CH, DeBerardinis RJ, Green GG, Leach MO, Rajan SS, Rizi RR, Ross BD, Warren WS, Malloy CR. Analysis of cancer metabolism by imaging hyperpolarized nuclei: Prospects for translation to clinical research. Neoplasia. 2011; 13:81–97. [PubMed: 21403835]
5. Chen AP, Albers MJ, Cunningham CH, Kohler SJ, Yen Y-F, Hurd RE, Tropp J, Bok R, Pauly JM, Nelson SJ, Kurhanewicz J, Vigneron DB. Hyperpolarized C-13 spectroscopic imaging of the TRAMP mouse at 3T-initial experience. Magn Reson Med. 2007; 58:1099–1106. [PubMed: 17969006]
6. Albers MJ, Bok R, Chen AP, Cunningham CH, Zierhut ML, Zhang VY, Kohler SJ, Tropp J, Hurd RE, Yen Y-F, Nelson SJ, Vigneron DB, Kurhanewicz J. Hyperpolarized 13C lactate, pyruvate, and

alanine: noninvasive biomarkers for prostate cancer detection and grading. Cancer Res. 2008; 68:8607–8615. [PubMed: 18922937]

7. Darpolor MM, Yen Y-F, Chua M-S, Xing L, Clarke-Katzenberg RH, Shi W, Mayer D, Josan S, Hurd RE, Pfefferbaum A, Senadheera L, So S, Hofmann LV, Glazer GM, Spielman DM. In vivo MRSI of hyperpolarized [1-(13)C]pyruvate metabolism in rat hepatocellular carcinoma. NMR Biomed. 2011; 24:506–513. [PubMed: 21674652]
8. Day SE, Kettunen MI, Gallagher FA, Hu D-E, Lerche M, Wolber J, Golman K, Ardenkjaer-Larsen JH, Brindle KM. Detecting tumor response to treatment using hyperpolarized 13C magnetic resonance imaging and spectroscopy. Nat Med. 2007; 13:1382–1387. [PubMed: 17965722]
9. Witney TH, Kettunen MI, Hu D-e, Gallagher FA, Bohndiek SE, Napolitano R, Brindle KM. Detecting treatment response in a model of human breast adenocarcinoma using hyperpolarised [1-13C]pyruvate and [1,4-13C2]fumarate. Br J Cancer. 2010; 103:1400–1406. [PubMed: 20924379]
10. Day SE, Kettunen MI, Cherukuri MK, Mitchell JB, Lizak MJ, Morris HD, Matsumoto S, Koretsky AP, Brindle KM. Detecting response of rat C6 glioma tumors to radiotherapy using hyperpolarized [1-13C]pyruvate and 13C magnetic resonance spectroscopic imaging. Magn Reson Med. 2011; 65:557–563. [PubMed: 21264939]
11. Saito K, Matsumoto S, Devasahayam N, Subramanian S, Munasinghe JP, Morris HD, Lizak MJ, Ardenkjaer-Larsen JH, Mitchell JB, Krishna MC. Transient decrease in tumor oxygenation after intravenous administration of pyruvate. Magn Reson Med. 2012; 67:801–807. [PubMed: 22006570]
12. Park I, Larson PEZ, Zierhut ML, Hu S, Bok R, Ozawa T, Kurhanewicz J, Vigneron DB, VandenBerg SR, James CD, Nelson SJ. Hyperpolarized 13C MR metabolic imaging: application to brain tumors. Neuro Oncol. 2010; 12:133–44. [PubMed: 20150380]
13. Park I, Bok R, Ozawa T, Phillips JJ, James CD, Vigneron DB, Ronen SM, Nelson SJ. Detection of early response to temozolomide treatment in brain tumors using hyperpolarized 13C MR metabolic imaging. J Magn Reson Imaging. 2011; 33:1284–1290. [PubMed: 21590996]
14. Hu S, Balakrishnan A, Bok RA, Anderton B, Larson PEZ, Nelson SJ, Kurhanewicz J, Vigneron DB, Goga A. 13C-pyruvate imaging reveals alterations in glycolysis that precede c-Myc-induced tumor formation and regression. Cell Metab. 2011; 14:131–142. [PubMed: 21723511]
15. Merritt ME, Harrison C, Storey C, Sherry AD, Malloy CR. Inhibition of carbohydrate oxidation during the first minute of reperfusion after brief ischemia: NMR detection of hyperpolarized 13CO2 and H13CO3- Magn Reson Med. 2008; 60:1029–1036. [PubMed: 18956454]
16. Schroeder MA, Cochlin LE, Heather LC, Clarke K, Radda GK, Tyler DJ. In vivo assessment of pyruvate dehydrogenase flux in the heart using hyperpolarized carbon-13 magnetic resonance. Proc Natl Acad Sci U S A. 2008; 105:12051–12056. [PubMed: 18689683]
17. Chen AP, Hurd RE, Schroeder MA, Lau AZ, Gu Y-p, Lam WW, Barry J, Tropp J, Cunningham CH. Simultaneous investigation of cardiac pyruvate dehydrogenase flux, Krebs cycle metabolism and pH, using hyperpolarized [1,2-13C2]pyruvate in vivo. NMR Biomed. 2012; 25:305–311. [PubMed: 21774012]
18. MacKenzie JD, Yen Y-F, Mayer D, Tropp J, Hurd R, Spielman DM. Detection of inflammatory arthritis using hyperpolarized 13C-pyurvate with magnetic resonance imaging and spectroscopy. Radiology. 2011; 259:414–420. [PubMed: 21406626]
19. Nagashima K. Optimum pulse flip angles for multi-scan acquisition of hyperpolarized NMR and MRI. J Magn Reson. 2008; 190:183–188. [PubMed: 18023219]
20. Zhao L, Mulkern R, Tseng C-H, Williamson D, Patz S, Kraft R, Walsworth RL, Jolesz FA, Albert MS. Gradient-Echo Imaging Considerations for Hyperpolarized 129Xe MR. J Magn Reson B. 1996; 113:179–183.
21. Larson PEZ, Kerr AB, Chen AP, Lustig MS, Zierhut ML, Hu S, Cunningham CH, Pauly JM, Kurhanewicz J, Vigneron DB. Multiband excitation pulses for hyperpolarized 13C dynamic chemical-shift imaging. J Magn Reson. 2008; 194:121–127. [PubMed: 18619875]
22. Larson PEZ, Bok R, Kerr AB, Lustig M, Hu S, Chen AP, Nelson SJ, Pauly JM, Kurhanewicz J, Vigneron DB. Investigation of Tumor Hyperpolarized [1-13C]-Pyruvate Dynamics using Time-Resolved Multiband RF Excitation Echo-planar MRSI. Magn Reson Med. 2010; 63:582–591. [PubMed: 20187172]

23. Larson PEZ, Hu S, Lustig M, Kerr AB, Nelson SJ, Kurhanewicz J, Pauly JM, Vigneron DB. Fast dynamic 3D MR spectroscopic imaging with compressed sensing and multiband excitation pulses for hyperpolarized 13C studies. Magn Reson Med. 2011; 65:610–619. [PubMed: 20939089]
24. Harrison C, Yang C, Jindal A, DeBerardinis RJ, Hooshyar MA, Merritt M, Dean Sherry A, Malloy CR. Comparison of kinetic models for analysis of pyruvate-to-lactate exchange by hyperpolarized 13 C NMR. NMR Biomed. 2012; 25:1286–1294. [PubMed: 22451442]
25. Lau AZ, Chen AP, Barry J, Graham JJ, Dominguez-Viqueira W, Ghugre NR, Wright GA, Cunningham CH. Reproducibility study for free-breathing measurements of pyruvate metabolism using hyperpolarized (13) C in the heart. Magn Reson Med. 2013; 69:1063–1071. [PubMed: 22760647]
26. Schulte RF, Sperl JI, Weidl E, Menzel MI, Janich MA, Khegai O, Durst M, Ardenkjaer-Larsen JH, Glaser SJ, Haase A, Schwaiger M, Wiesinger F. Saturation-recovery metabolic-exchange rate imaging with hyperpolarized [1-(13) C] pyruvate using spectral-spatial excitation. Magn Reson Med. 2013; 69:1209–1216. [PubMed: 22648928]
27. Kerr, AB.; Larson, PE.; Lustig, M.; Cunningham, CH.; Chen, AP.; Vigneron, DB.; Pauly, JM. Multiband Spectral-Spatial Design for High-Field and Hyperpolarized C-13 Applications; Proceedings of the 16th Annual Meeting of ISMRM; 2008. p. 226
28. Harris T, Eliyahu G, Frydman L, Degani H. Kinetics of hyperpolarized 13C1-pyruvate transport and metabolism in living human breast cancer cells. Proc Natl Acad Sci U S A. 2009; 106:18131–18136. [PubMed: 19826085]
29. Zierhut ML, Yen Y-F, Chen AP, Bok R, Albers MJ, Zhang V, Tropp J, Park I, Vigneron DB, Kurhanewicz J, Hurd RE, Nelson SJ. Kinetic modeling of hyperpolarized 13C1-pyruvate metabolism in normal rats and TRAMP mice. J Magn Reson. 2010; 202:85–92. [PubMed: 19884027]
30. Derby K, Tropp J, Hawryszko C. Design and evaluation of a novel dual-tuned resonator for spectroscopic imaging. J Magn Reson. 1990; 86:256–262.
31. Cunningham CH, Chen AP, Albers MJ, Kurhanewicz J, Hurd RE, Yen Y-F, Pauly JM, Nelson SJ, Vigneron DB. Double spin-echo sequence for rapid spectroscopic imaging of hyperpolarized 13C. J Magn Reson. 2007; 187:357–362. [PubMed: 17562376]
32. Wilson DM, Keshari KR, Larson PEZ, Chen AP, Criekinge MV, Bok R, Nelson SJ, Macdonald JM, Vigneron DB, Kurhanewicz J. Multi-compound Polarization by DNP Allows Simultaneous Assessment of Multiple Enzymatic Activities In Vivo. J Magn Reson. 2010; 205:141–147. [PubMed: 20478721]
33. Swisher CL, Larson PEZ, Kruttwig K, Kerr AB, Hu S, Bok RA, Goga A, Pauly JM, Nelson SJ, Kurhanewicz J, Vigneron DB. Quantitative measurement of cancer metabolism using stimulated echo hyperpolarized carbon-13 MRS. Magn Reson Med. 2013 Available online ahead of print.
34. Cunningham CH, Chen AP, Lustig M, Hargreaves BA, Lupo J, Xu D, Kurhanewicz J, Hurd RE, Pauly JM, Nelson SJ, Vigneron DB. Pulse sequence for dynamic volumetric imaging of hyperpolarized metabolic products. J Magn Reson. 2008; 193:139–146. [PubMed: 18424203]

Highlights

- Two new variable flip angle schemes for hyperpolarized MR
- Account for exchange/conversion between different compounds
- Multi-band RF pulses used for frequency specific flip angles
- In vivo hyperpolarized carbon-13 results show improved SNR and temporal window

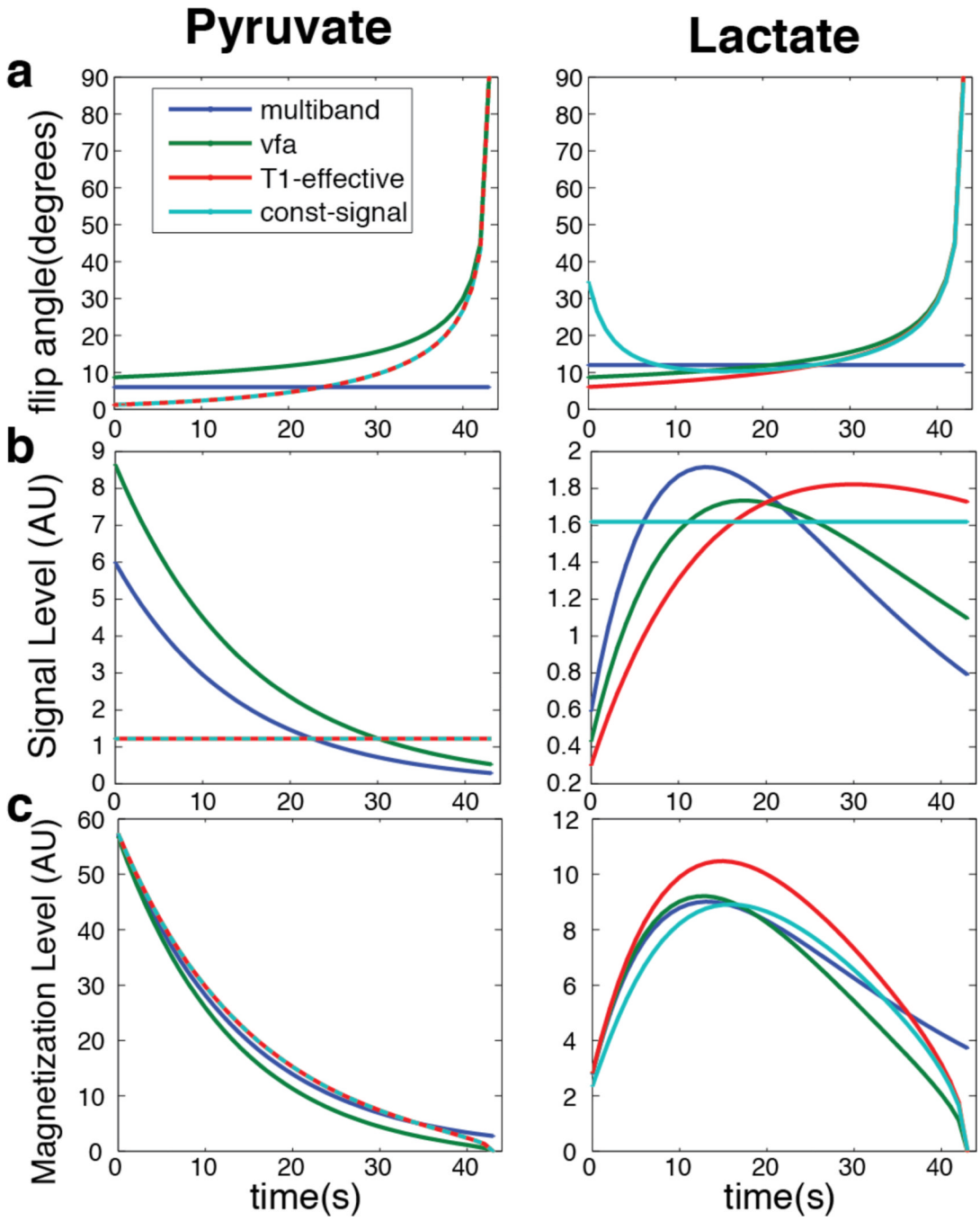

Figure 1.

Comparison of multiband constant in time scheme ("*multiband*"), variable flip angle - constant between metabolites without metabolic conversion or T_1 ("*vfa*"), optimized scheme using effective relaxation rates ("*T1-effective*"), and optimized scheme for constant signal ("*const-signal*"), the last two using $K_{PL} = 0.025\ s^{-1}$ and $P(0) = 1$ and $L(0) = 0.05$, and $T_{1P} = T_{1L} = 25$ s. (a) Flip angle variation over time. Simulated (b) signal curves and (c) remaining magnetization. Note that the pyruvate flip angles and simulated signal are the same for the *T1-effective* and *const-signal* schemes.

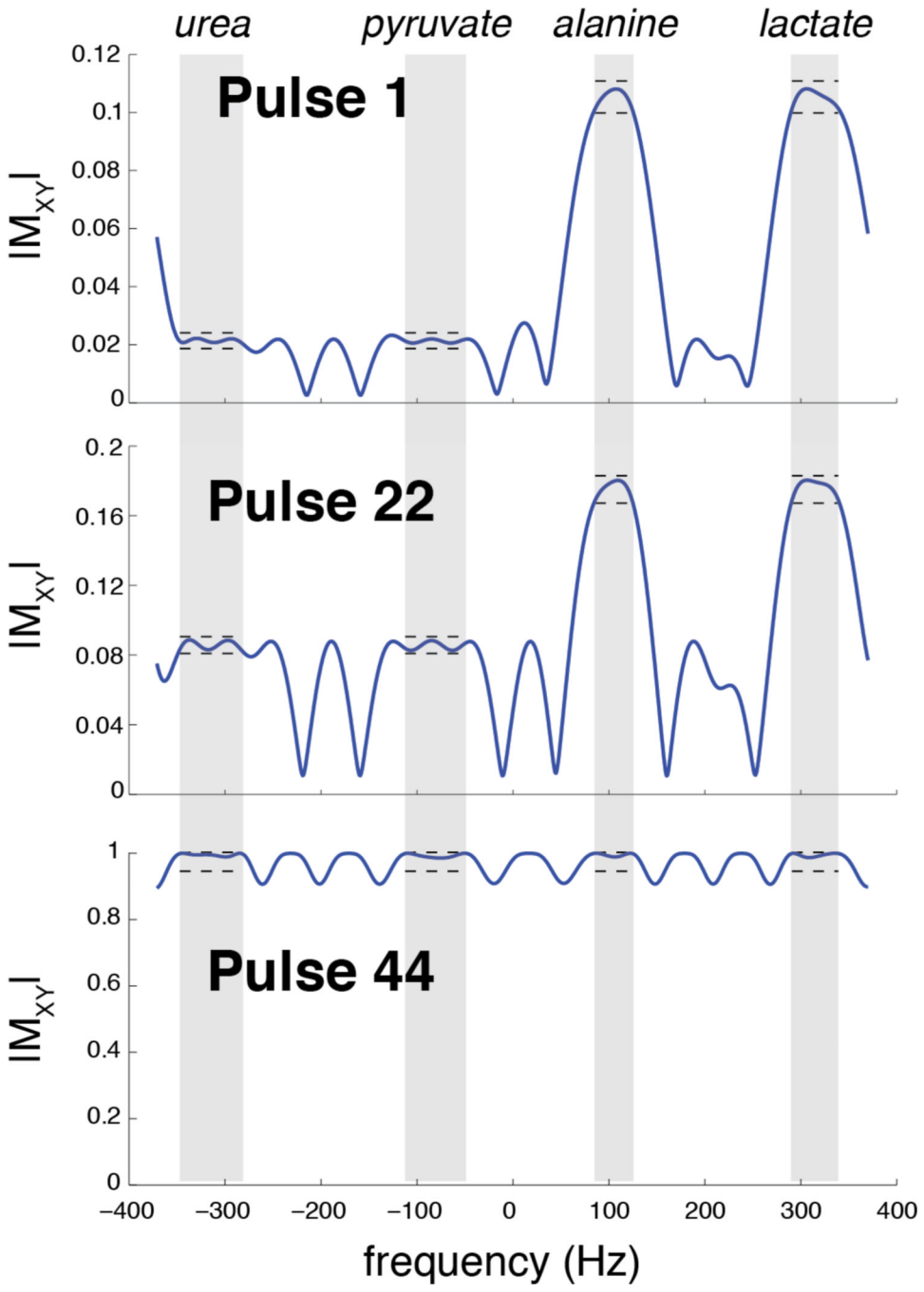

Figure 2.

Sample spectral-spatial RF pulse spectral profiles for the 1st, 22nd, and 44th pulses out of 44 total RF pulses designed for the *T1-effective* scheme in Fig. 1. The urea flip angle was set to be the same as pyruvate and the alanine flip angle to be the same as lactate. The dashed lines indicate the specified flip angle ranges.

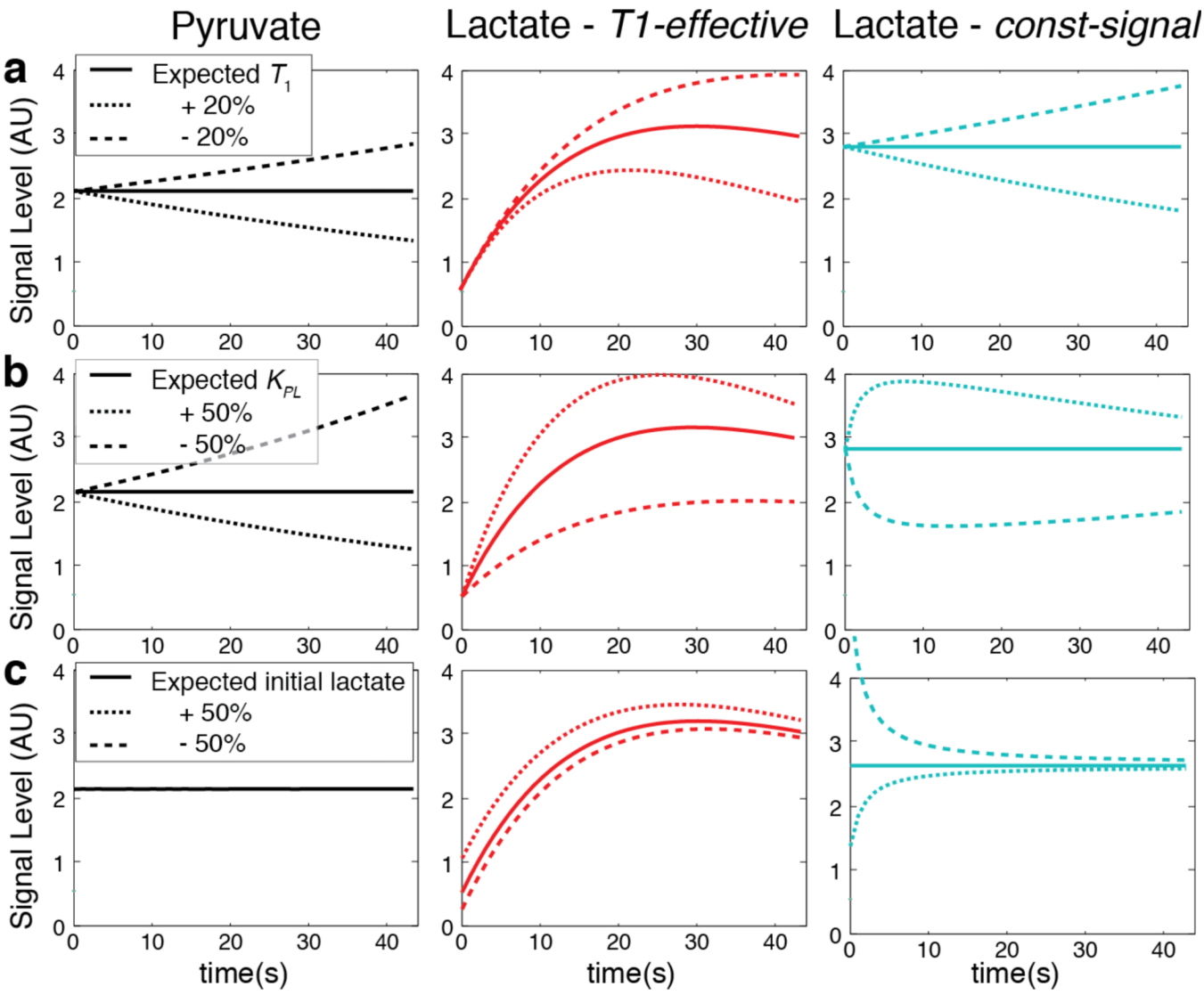

Figure 3.

Simulated signal when the (a) $T_1 = T_{1P} = T_{1L}$, (b) K_{PL}, and (c) initial lactate magnetization levels vary (dashed lines) from those used in the flip angle designs ("expected", solid lines) for the presented *T1-effective* and *const-signal* schemes. The flip angles used are shown in Fig. 1a as (the pyruvate flip angles are the same for both of these schemes).

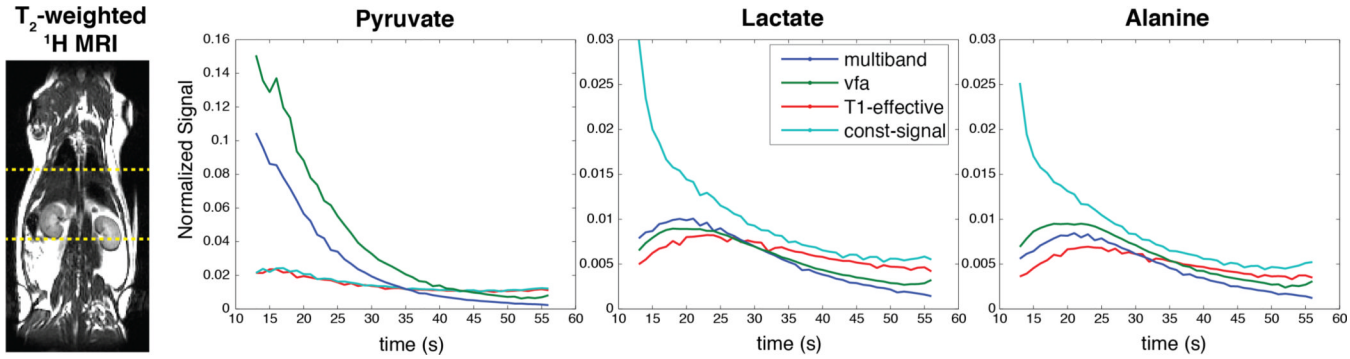

Figure 4.

Metabolite peak height dynamics following a [1-^{13}C]pyruvate injection in a 4 cm abdomen slab of a normal rat (left). The flip angle schemes used are shown in Fig. 1.

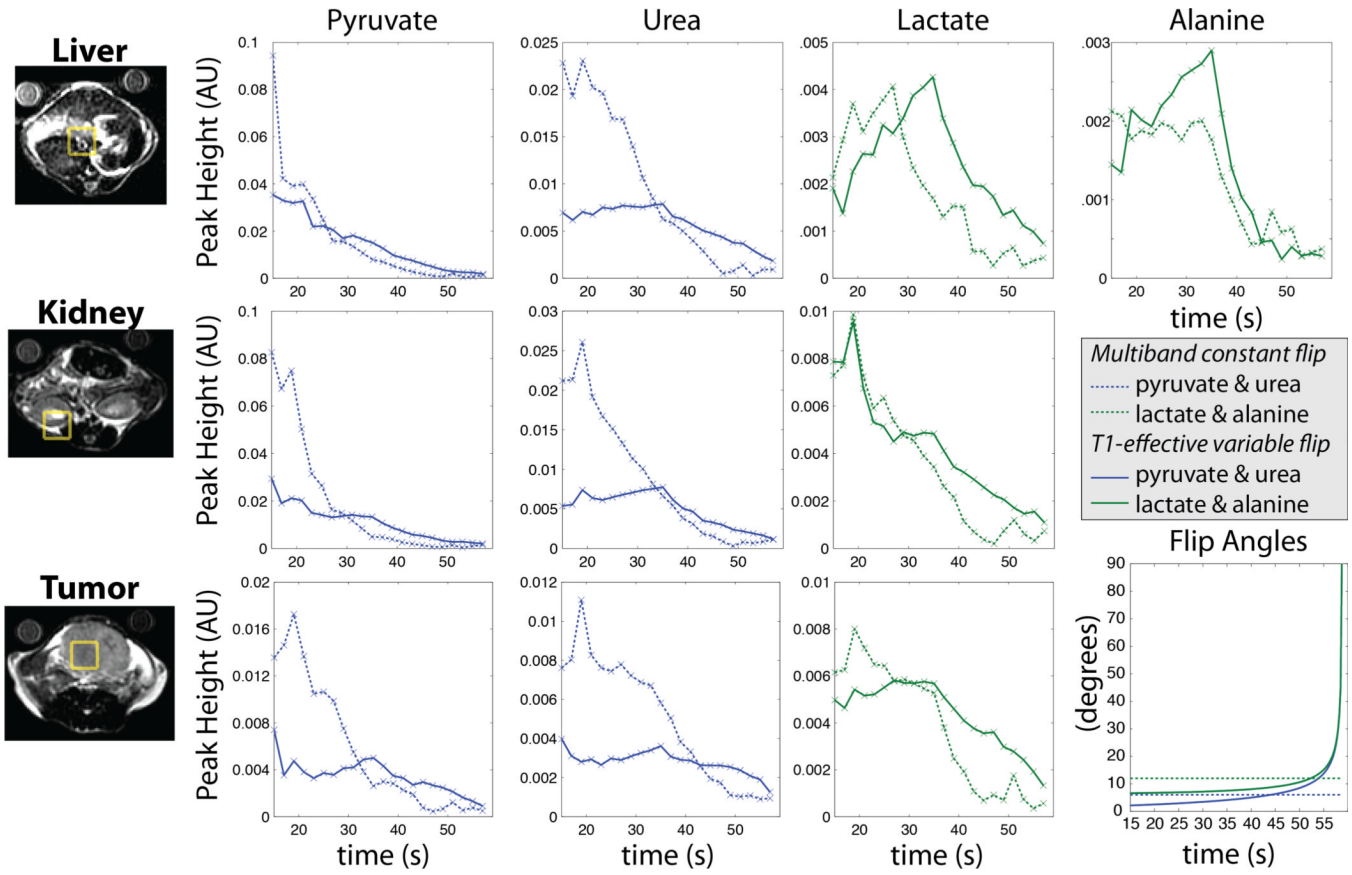

Figure 5.

Dynamic 3D-MRSI in a transgenic prostate tumor mouse model (TRAMP) with 2-s time resolution. A *T1-effective* dynamic variable flip angle scheme was generated using K_{PL} = 0.025 1/s, $T_{1P} = T_{1L} = \infty$, 44 s total acquisition time, and compared to a constant 6 (pyruvate & urea) and 12 (lactate & alanine) degree multiband excitation [23].

Table 1

Kinetic model fits to the data in Fig. 4. For an accurate comparison to the parameters used in the flip angle design, both metabolic products of lactate and alanine have been summed together for the fitting (X=L+A) since they received the same flip angles. The data was normalized such that $P(0) = 1$.

	T_{1P}	T_{1X}	k_{PX}	$X(0)$
Design parameters	25	25	0.025	0.05
multiband	13.0	13.7	0.0146	0.0596
vfa	13.8	13.1	0.0156	0.0901
T1-effective	13.9	14.3	0.0153	0.0837
const-signal	16.0	12.0	0.0252	0.0920